[8]J. A. Cape and J. M. Zimmerman, Phys. Rev. 153, 416 (1967).
[9]S. T. Sekula and R. H. Kernohan, J. Phys. Chem. Solids 27, 1863 (1966).
[10]G. Bon Mardion, B. B. Goodman, and A. Lacaze, J. Phys. Chem. Solids 26, 1143 (1965).
[11]B. B. Goodman, IBM J. Res. Develop. 6, 62 (1962).
[12]C. Caroli, M. Cyrot, and P. G. de Gennes, Solid State Commun. 4, 17 (1966).
[13]E. Helfand and N. R. Werthamer, Phys. Rev. 147, 288 (1966).
[14]G. Eilenberger, Phys. Rev. 153, 584 (1967).
[15]G. Cody, in Proceedings of the 1968 Summer Study of Superconducting Devices and Accelerators, Brookhaven National Laboratory, Part II, p. 406 (unpublished).
[16]D. K. Finnemore, T. F. Stroudsberg, and C. A. Swenson, Phys. Rev. 149, 231 (1966).
[17]W. F. Brown, Jr., *Magnetostatic Principles in Ferromagnetism* (North-Holland, Amsterdam, 1962), Appendix, p. 187.
[18]P. S. Swartz and H. R. Hart, Jr., Phys. Rev. 137, A818 (1965).

PHYSICAL REVIEW B VOLUME 2, NUMBER 5 1 SEPTEMBER 1970

Collective Excitation Spectroscopy in Superconductor-Semiconductor Tunnel Junctions*

C. B. Duke
Department of Physics, Materials Reasearch Laboratory, and Coordinated Science Laboratory, University of Illinois, Urbana, Illinois 61801
and
G. G. Kleiman
Department of Physics and Materials Research Laboratory, University of Illinois, Urbana, Illinois 61801
(Received 19 December 1969)

The transfer-Hamiltonian description of the influence of electron-boson interactions on the electrical characteristics of metal-semiconductor tunnel junctions is extended by considering the combined effects of electrode self-energy phenomena and boson-assisted tunneling. The current associated with these processes is evaluated for superconducting metal electrodes described by the pairing model as well as for normal metal electrodes. Numerical evaluations of the conductance are made using models and parameters appropriate for the description of the influence of electron (hole) interactions with optical phonons (energy $\cong \hbar\omega_0$) on the tunneling characteristics of metal contacts on boron-doped silicon.

I. INTRODUCTION

In the past few years, the transfer-Hamiltonian description[1,2] of electron tunneling in solids has been extended[3-9] and shown to be capable of describing qualitatively the various types of many-body effects which have been observed in tunnel junctions[6] (with the sole exception of tunneling through real intermediate states[6,10,11]). In this paper we report two new extensions of this description: the simultaneous consideration both in inelastic tunneling and of electrode self-energy effects, and the study of these phenomena in metal-semiconductor tunnel junctions in which the metal electrode is a superconductor.

To understand the motivation for the importance of these extensions, let us recall some of the main features of the transfer-Hamiltonian description of the influence of electron-phonon coupling in the semiconductor on the conductance characteristics of metal-semiconductor tunnel junctions. The essence of this description is that once a set of basis states for the "electrode" wave function have been selected, the junction Hamiltonian can be written formally as

$$\mathcal{H} = \mathcal{H}_L + \mathcal{H}_R + \mathcal{H}_T \ , \tag{1.1}$$

in which $\mathcal{H}_L$ and $\mathcal{H}_R$ describe matrix elements between states in the left- and right-hand electrodes, respectively, and $\mathcal{H}_T$ describes matrix elements which transfer an electron from one electrode to the other. The tunneling current is evaluated by a straightforward linear response analysis in which $\mathcal{H}_T$ is treated as the "external" source.[6] This analysis permits us to introduce a diagrammatic description of the tunnel current[6] analogous to that of the linear-response theory of electrical conductivity.[12,13] The diagrammatic analysis is developed in detail in Refs. 4 and 6. Therefore, in Fig. 1 we merely present some of the relevant diagrams for the current. Figure 1(a) specifies the elastic current which, if an independent electron model is used to describe both metal and semiconductor, reduces to the ordinary one-electron current through a potential barrier.[6] Davis and Duke[7,14] extended the analysis of this diagram

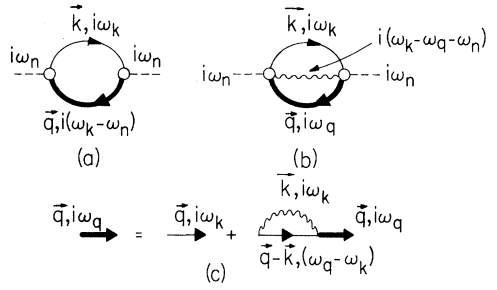

FIG. 1. (a) Elastic tunneling diagram for tunneling in a metal-semiconductor junction with a coherent tunneling vertex, $\Lambda_{\vec{k}\vec{q}}^{(0,0)}(i\omega_n)$, and self-energy corrections in the semiconductor electrode described by the $\vec{q}$, $i(\omega_k - \omega_n)$ variables. The metal electrode, described by $\vec{k}$, $i\omega_k$, can be either normal or superconducting. (b) Single-boson-emission inelastic tunneling diagram with a coherent tunneling vertex, $\Lambda_{\vec{k}\vec{q}}^{(0,1)}$ $(\vec{p}, i\omega_n)$ and self-energy corrections in the semiconductor electrode $(\vec{q}, i\omega_q)$. The metal electrode $(\vec{k}, i\omega_k)$ can be either normal or superconducting. (c) Dyson's equation describing our approximation to electron-boson coupling in the semiconductor electrode. All notation is that used by Duke (Ref. 6).

to include phonon self-energy effects in the semiconductor electrode, and Duke, Rice, and Steinrisser[15] similarly extended it to include plasmon self-energy effects. In this paper, we extend the Davis-Duke calculation to the case of BCS superconducting metal electrodes. Figure 1(b) designates single-boson-emission inelastic tunneling. It has been evaluated using noninteracting-electron models of the electrodes to describe phonon emission by Duke, Silverstein, and Bennett[3,4] and to describe plasmon emission by Ngai, Economou, and Cohen.[16] We extend the analysis of Duke *et al.* by generalizing to the case of superconducting metal electrodes, and by considering phohon-assisted tunneling for both normal and superconducting electrodes in the presence of phonon self-energy effects in the semiconductor electrode. Figure 1(c) designates our approximate treatment of electron-phonon interactions in the semiconductor electrode.

Having noted the technical aspects of our extensions of the transfer-Hamiltonian model, let us next inquire why these extensions can be of more than routine interest. A basic aspect[6] of the transfer-Hamiltonian model is its dependence on an *a priori* definition of a set of basic states to define the decomposition of the Hamiltonian given in Eq. (1.1). Therefore, many of its predictions may not be unique consequences of the particular microscopic model originally used to formulate them. Consequently, the identification of particular line-shape phenomena observed in experimental data with a particular microscopic mechanism rests upon the adequacy (or lack thereof) of independent checks that the features of the line shape predicted by this mechanism are (a) unique and (b) faithfully mirrored in the data. In the case of simple models, we usually can satisfy requirement (a) as noted in Fig. 2 for the distinction between inelastic tunneling [Fig. 1(b)] and self-energy effects [Fig. 1(a)]. The model[6] used to obtain the figure embodies deformation-potential coupling of the electron to dispersionless optical phonons, the quasiparticle approximation to describe the semiconductor in a metal-semiconductor contact, and the free-electron model for the metal electrons. In this simple case, the distinction between "steps" and "cusps" as well as that between symmetry and antisymmetry about zero bias is clear and unambiguous. Unfortunately, this simplicity rarely is present in experimental data. It also disappears quickly as the model Hamiltonians are refined.[6,9] For example, momentum dependence of the electron-boson vertex can invert the reverse bias ($eV < 0$) cusp[15] in Fig. 2, thereby destroying the symmetry distinction between the two mechanisms, while boson dispersion spreads out both line shapes,[7,15,16] thereby mitigating the line-shape distinction. Even for narrow boson-dispersion curves, the onset of damping in the electrode propagator at the boson-emission threshold causes the self-energy line shape to exhibit some "step-like" behavior in addition to the quasiparticle cusps.[17] This is especially true at

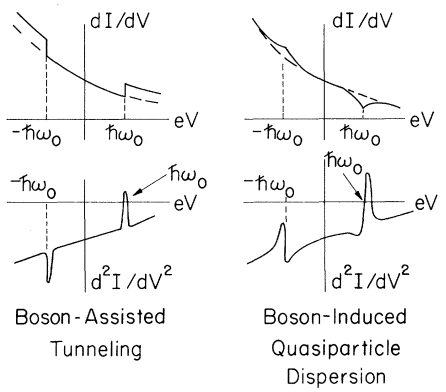

FIG. 2. Schematic illustration of the distinction between the tunneling characteristics associated with interactions in the barrier (described by $\mathcal{H}_T$ and labeled inelastic tunneling) and those associated with interactions in the electrodes (described by $\mathcal{H}_L$ and/or $\mathcal{H}_R$). The illustrated curves are drawn for a model of a metal-semiconductor contact in which interactions in the metal are neglected and the electrons in the semiconductor interact via a constant vertex function with dispersionless optical phonons as discussed by Davis and Duke (Ref. 7).

forward bias ($eV > 0$) when the simiconductor Fermi degeneracy ζ_R becomes nearly equal to the boson energy $\hbar\omega_0$. In this case, the self-energy and inelastic tunneling line shapes of $eV \cong \hbar\omega_0$ may be almost identical (although this is rarely true at reverse bias, $eV \cong -\hbar\omega_0$). Because of the possible ambiguity between the line-shape interpretations based on these two mechanisms, we decided to see if the change in the line shape when the metal electrode becomes superconducting could distinguish between the two mechanism in some of these ambiguous situations. It appears that such a distinction indeed is possible. However, existing data on even the best metal-insulator-silicon: B junctions[18] have not yet been refined sufficiently to permit a definitive interpretation. In addition, the distinctions predicted by existing model calculations are only slightly larger than the discrepancy between the calculated and experimental tunnel characteristics in a given sample. Consequently, the story is not yet fully told, although the general outline of the type of results which can be expected on the basis of the phenomenological transfer Hamiltonian model has been established.

In the body of the paper, our analysis is presented in three stages. Section II contains a synopsis of the final formulas describing both elastic and boson-assisted tunneling in superconductor-semiconductor junctions. Since the details of the calculations are routine,[6] they are omitted. In Sec. III, the numerical consequences of the general results are presented for metal contacts on p-type silicon. The sensitivity of the theoretical predictions on the construction and parameters of the models is examined in detail. Model-independent features of the results are identified and suggested for use as diagnostic probes for the identification of the mechanisms causing observed line shapes. Finally, Sec. IV contains a synopsis of the results and their comparison with experimental data for Pb contacts on Si:B. This Introduction, the figures, and Sec. IV provide a self-contained description of the main features of our results.

II. CLASSIFICATION AND EVALUATION OF CONTRIBUTIONS TO CURRENT

A. Self-Energy Effects

The contributions to the current associated with self-energy effects, which result from electron-phonon interaction terms in the semiconductor-electrode Hamiltonian rather than in the transfer Hamiltonian $\mathcal{H}_T$, are described diagrammatically in Fig. 1(a). The elastic current J_e, through the barrier is given by [4-6]

$$J_e(V,T) = -\frac{4e}{\hbar}\sum_{\vec{k},\vec{q}}\int_{-\infty}^{\infty}\frac{dx}{\pi}\,[n(x)-n(x-eV)] \times \mathrm{Im}G_L^R(\vec{k},x)\,\mathrm{Im}G_R^R(\vec{q},x-eV)\,|\Lambda_{\vec{k},\vec{q}}(x)|^2 , \quad (2.1)$$

$$n(x) = [1+e^{x/\kappa T}]^{-1} , \quad (2.2)$$

$$G_\alpha^R = \mathrm{Re}G_\alpha^R + i\,\mathrm{Im}G_\alpha^R . \quad (2.3)$$

In Eq. (2.2) we have used κ to denote Boltzmann's constant and T to denote the temperature. We adopt the convention that the right-hand electode is a semiconductor described by wave-vectors $\vec{q}$ and Fermi degeneracy ζ_R, whereas the left-hand electrode is a metal (either superconducting or normal) with Fermi degeneracy ζ_L and wave vectors $\vec{k}$. All energies are measured relative to the semiconductor Fermi level.

We use the pairing model[6] to describe superconductivity in the metal electrode:

$$\mathrm{Im}G_L^R(\vec{k},\epsilon) = -\pi\{u_k^2\,\delta[\epsilon - E(k)] + v_k^2\,\delta[\epsilon + E(k)]\} , \quad (2.4a)$$

$$\xi_{\vec{k}} = \hbar^2k^2/2m_L - \zeta_L , \quad (2.4b)$$

$$u_k^2 = \tfrac{1}{2}[1 + \xi_{\vec{k}}/(\xi_{\vec{k}}^2+\Delta^2)^{1/2}] , \quad (2.4c)$$

$$v_k^2 = \tfrac{1}{2}[1 - \xi_{\vec{k}}/(\xi_{\vec{k}}^2+\Delta^2)^{1/2}] , \quad (2.4d)$$

$$E(k) = (\xi_{\vec{k}}^2+\Delta^2)^{1/2} . \quad (2.4e)$$

Normal-metal results are recovered by setting $\Delta = 0$.

We also use the one-electron formula,[6]

$$|\Lambda_{\vec{k},\vec{q}}^{(0)}(\epsilon)|^2 = \frac{\partial\xi_{\vec{q}}}{\partial q_\perp}\frac{\partial\xi_{\vec{k}}}{\partial k_\perp}\,D(\vec{q}_\parallel,\epsilon)\,\delta_{\vec{k}_\parallel,\vec{q}_\parallel} , \quad (2.5)$$

for specular tunneling, where D is the one-electron barrier-penetration probability $\xi_{\vec{q}} = \hbar^2/2m_R - \zeta_R$, and $\vec{k}_\parallel$ and $\vec{q}_\parallel$ are the components of $\vec{k}$ and $\vec{q}$, respectively, parallel to the plane of the junction. After inserting (2.4) and (2.5) in (2.1), and letting $D(\vec{q}_\parallel,\epsilon) = D(E_\parallel,\epsilon)$, where $E_\parallel = \hbar^2q_\parallel^2/2m_R$, we obtain our final expression for the elastic current,

$$J_e(V,T) = \frac{4e\rho_\parallel}{h2\pi}\int_{-\zeta_R}^{\infty}d\xi_{\vec{q}}\int_0^{\xi_{\vec{q}}+\zeta_R}dE_\parallel\int_{-\infty}^{\infty}dx \times[n(x)-n(x-eV)]\,\mathrm{Im}G_R^R(\vec{q},x-eV) \times N_s(x)[\theta(x-\Delta)-\theta(-x-\Delta)]D(E_\parallel,x) , \quad (2.6a)$$

$$N_x(x) \equiv x/(x^2-\Delta^2)^{1/2} , \quad (2.6b)$$

where $\theta(x)$ is the unit step function.

The influence on the tunneling characteristics of the electron–optical-phonon interactions in the semiconductor electrode depends on (a) the momentum dependence of the electron-phonon vertex; (b) the background one-electron characteristics as reflected in $D(E_\parallel,x)$ and the phase-space restrictions on the $E_\parallel$ integral; and (c) the onset of an increased energy width in the one-electron propagator at the optical-phonon threshold energy. A convenient description of effects (a) and (b) can be given within the framework of the quasiparticle

approximation defined by

$$\mathrm{Im}G_R^R(\vec{q}, x) = -Z(x)\pi\delta[\xi_{\vec{q}} - \xi(x)] \ , \tag{2.7a}$$

$$x - \xi(x) - \mathrm{Re}\Sigma(\xi(x), x) = 0 \ , \tag{2.7b}$$

$$Z(x) = [1 + \partial \mathrm{Re}\Sigma(\xi_{\vec{q}}, x)/\partial\xi_{\vec{q}}]^{-1}_{\xi_{\vec{q}} = \xi(x)} . \tag{2.7c}$$

As usual, $\Sigma(\xi_{\vec{q}}, x)$ designates the retarded electronic proper self-energy, which has been specified explicitly by Davis and Duke[7] for a variety of electron-phonon coupling mechanisms. A classification of the generic effects of different types of electron-phonon coupling on the tunneling characteristics has been given by Duke.[9] For optical phonons in homopolar materials (silicon and germanium), $\Sigma(\xi_{\vec{q}}, \epsilon)$ depends only on ϵ. In this case, if $D(E_{\|}, x) = D_0(E_{\|})$ is a function of $E_{\|}$ alone, which occurs in the constant-barrier and uniform-field models of the barrier, then use of (2.7) in (2.6) gives

$$\begin{aligned} G_e(V, T) &\equiv \frac{dJ_e(V, T)}{d(eV)} \\ &= -\frac{2e\rho_{\|}}{h}\left\{-\int_{x(-\zeta_R)}^{-eV-\Delta} dx\, S_1(x, eV) \right. \\ &\quad \times \theta[-eV - \Delta - x(-\zeta_R)] \\ &\quad + \int_{-eV+\Delta}^{\infty} dx\, S_1(x, eV) \\ &\quad \times \theta[-eV + \Delta - x(-\zeta_R)] \\ &\quad + \int_{x(-\zeta_R)}^{\infty} dx\, S_1(x, eV) \\ &\quad \left. \times \theta[x(-\zeta_R) + eV - \Delta]\right\} \ , \end{aligned} \tag{2.8a}$$

$$S_1(x, eV) \equiv \{\xi'(x) D_0[\xi(x) + \zeta_R][n(x + eV) - n(x)] - \int_0^{\xi(x)+\zeta_R} dE_{\|} D_0(E_{\|}) n'(x)\} N_s(x + eV) \ , \tag{2.8b}$$

$$\rho_{\|} \equiv m_R/2\pi\hbar^2 \ , \tag{2.8c}$$

$$n'(y) \equiv dn(y)/dy, \quad \xi'(y) \equiv d\xi(y)/dy \ , \tag{2.8d}$$

where $N_s(x)$ is defined by Eq. (2.6b), and $x(-\zeta_R)$ is the negative of the renormalized Fermi degeneracy satisfying

$$x(-\zeta_R) + \zeta_R - \mathrm{Re}\Sigma[x(-\zeta_R)] = 0 \ .$$

In general, we shall consider D_0 to be a function of $E_{\|}$ only, but include the effects of the abrupt increase in $\mathrm{Im}\Sigma(\epsilon)$ at $|\epsilon| \geq \hbar\omega_0$. At $T = 0$, using the free-electron model of the semiconductor Eq. (2.8a) reduces, in the constant-barrier model[6] ($D \to D_0$), to

$$\begin{aligned} G_e(V, 0) &= (2e\rho_{\|}/h) D_0 \{c_1(eV, \zeta_R) \\ &\quad \times [\theta(-eV - \Delta) - \theta(eV - \Delta)\theta(\zeta_R - eV + \Delta)] \\ &\quad - [c_1(eV, \zeta_R) - c_1(eV + \zeta_R, 0)] \\ &\quad \times \theta(-\zeta_R + eV - \Delta)\} \ , \end{aligned} \tag{2.9a}$$

$$c_1(x, y) \equiv +(x^2 - \Delta^2)^{1/2} - yx/(x^2 - \Delta^2)^{1/2} \ . \tag{2.9b}$$

Equations (2.8) illustrate clearly the influence which superconductivity in the metal eletrode exerts on the line shape due to self-energy effects in the semiconductor. The peaks in the superconducting density of states at $x = \pm\Delta$ strongly weight the contributions to the conductance from the quasiparticle peaks in $\xi(x)$ at values of the bias $eV \cong \pm(\hbar\omega_0 + \Delta)$. This effect is illustrated schematically in Fig. 3 where it is seen to lead to a shift in the cusp structure in the conductance to larger values of the bias in superconductor-semiconductor junctions relative to normal-metal–semiconductor junctions. The sharp maximum in $x(x^2 - \Delta^2)^{-1/2}$ at $x = \pm\Delta$ also leads to a sharpening of the cusp structure in superconductor-semiconductor contacts. Either phonon dispersion or quasiparticle damping broadens the structure and reduces both the shift and sharpening.

To account for the abrupt size rise in $\mathrm{Im}\Sigma$ at $|\epsilon| \geq \hbar\omega_0$, we consider the constant-barrier-penetration model by setting $D = D_0$ while retaining the full $\mathrm{Im}G^R(\xi, x)$ in Eq. (2.6). We obtain

$$\begin{aligned} J_e(V, T) &= -\frac{2e\rho_{\|}}{h} D_0 \int_{-\infty}^{\infty} \frac{dx}{\pi}[n(x) - n(x - eV)] \\ &\quad \times N_s(x)[\theta(x - \Delta) - \theta(-x - \Delta)] Y(x - eV) \ , \end{aligned} \tag{2.10a}$$

where

$$Y(x) = \frac{|\mathrm{Im}\Sigma(x)|}{2} \ln\left(\frac{E_0^2 + [\mathrm{Im}\Sigma(x)]^2}{[\zeta_R + \xi(x)]^2 + [\mathrm{Im}\Sigma(x)]^2}\right)$$

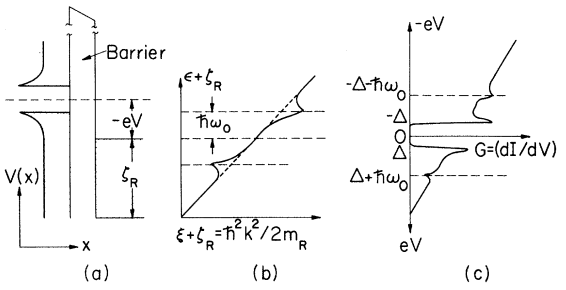

FIG. 3. (a) Schematic potential versus distance diagram of a superconductor-semiconductor tunnel junction. Forward bias ($eV > 0$) is defined when the metal is biased positively relative to the semiconductor. (b) Dispersion relation for electrons in the degenerate n-type semiconductor electrode interaction with dispersionless optical phonons of energy $\hbar\omega_0$. The dashed line indicates the dispersion relation in the absence of electron-phonon interactions. (c) The tunnel conductance at zero temperature of the metal-semiconductor tunnel junction shown in Fig. 3(a). The constant-barrier-penetration model is used in evaluating the G shown in the figure. The cusps at $eV \cong \pm(\hbar\omega_0 + \Delta)$ are sharper than they would have been for a normal-metal electrode.

$$+(\zeta_R+\xi(x))\left[\tfrac{1}{2}\pi+\tan^{-1}\left(\frac{\zeta_R+\xi(x)}{\mathrm{Im}\Sigma(x)}\right)\right] \quad , \tag{2.10b}$$

and E_0 is an energy cutoff to prevent divergence of the ξ_q integral. Taking the derivative of Eqs. (2.10) with respect to eV gives, for a constant D, the conductance

$$G_e(V,T)=\frac{2e\rho_{\parallel}}{h}D_0\left[\int_{-eV+\Delta}^{\infty}\frac{dy}{\pi}S_2(y,eV)-\int_{-\infty}^{-eV-\Delta}\frac{dy}{\pi}S_2(y,eV)\right] \quad , \tag{2.11a}$$

$$S_2(y,eV)\equiv\{[n(y+eV)-n(y)]Y'(y)-n'(y)Y(y)\}\times N_s(y+eV) \quad , \tag{2.11b}$$

$$Y'(y)\equiv dY(y)/dy \quad . \tag{2.11c}$$

Although the general features of the experimental line shape are reproduced by the quasiparticle approximation, the explicit treatment in Eq. (2.6) of the rapid changes in $\mathrm{Im}\Sigma$ improves some of the details, especially when $eV\cong(\hbar\omega_0+\Delta)$ and $\hbar\omega_0\cong\zeta_R$.

B. Phonon-Assisted Tunneling

The diagram for single-boson-assisted tunneling is shown in Fig. 1(b) in which solid lines denote free-electron propagators and the wavy line designates the propagator describing a boson created by the tunneling electron. In the presence of self-energy effects in either of the electrodes, the inelastic current J_i associated with this diagram is given by[4,6]

$$J_i(V,T)=-\frac{2e}{\hbar}\sum_{\vec{k}\alpha\vec{q}\beta}\int_{-\infty}^{\infty}\frac{dx\,dx'}{\pi^2}[n(x)-n(x+eV)]\times[n(x')+N(x'-x-eV)]\,\mathrm{Im}G^R_{\alpha L}(\vec{k},x')\times\mathrm{Im}G^R_{\beta R}(\vec{q},x)\,\mathrm{Im}\,D^R_{\vec{k}\alpha,\vec{q}\beta}(x'-x-eV) \quad , \tag{2.12}$$

$$N(x)=[e^{x/\kappa T}-1]^{-1} \quad , \tag{2.13}$$

$$D_{\vec{k}\alpha,\vec{q}\beta}(i\omega_l)\equiv[-\int_0^{1/\kappa T}d\tau\,\langle T_\tau[\Lambda^{(1)}_{\vec{k}\alpha,\vec{q}\beta}(\tau)\Lambda^{(1)}_{\vec{k}\alpha,\vec{q}\beta}(0)]\rangle e^{i\omega_l\tau}] \quad . \tag{2.14}$$

For noninteracting bosons,

$$D_{\vec{k}\alpha,\vec{q}\beta}(i\omega_l)=-\textstyle\sum_{\vec{p}}|\Lambda^{(0,1)}_{\vec{k}\vec{q}}(\vec{p})|^2\delta_{\alpha\beta}\left(\frac{-1}{i\omega_l-\hbar\omega_{\vec{p}}}+\frac{1}{i\omega_l+\hbar\omega_{\vec{p}}}\right) \quad , \tag{2.15a}$$

$$\mathrm{Im}\,D^R_{\vec{k}\alpha,\vec{q}\beta}(x)\equiv\mathrm{Im}\,D_{\vec{k}\alpha,\vec{q}\beta}(i\omega_l\to x+i\delta)=-\pi\textstyle\sum_{\vec{p}}|\Lambda^{(0,1)}_{\vec{k}\vec{q}}(\vec{p})|^2\delta_{\alpha\beta}\times[\delta(x-\hbar\omega_{\vec{p}})-\delta(x+\hbar\omega_{\vec{p}})]. \tag{2.15b}$$

In these equations $\hbar\omega_{\vec{p}}$ denotes the phonon energy.

If Eq. (2.4a) is used for the spectral weight in the superconductor, and we adopt the definition

$$|\Lambda^{(0,1)}_{\vec{k},\vec{q}}(\vec{p})|^2\equiv|\Lambda^{(i)}(\vec{p})|^2\frac{\partial\xi_{\vec{q}}}{\partial q_\perp}\frac{\partial\xi_{\vec{k}}}{\partial k_\perp}\delta_{\vec{k}_\parallel,\vec{q}_\parallel} \quad , \tag{2.16}$$

then we obtain

$$J_i(V,T)=-\frac{2(2s+1)e}{h}\sum_{\vec{p},\vec{q}}|\Lambda^{(i)}(\vec{p})|^2\frac{\partial\xi_{\vec{q}}}{\partial q_\perp}\times\int_{-\infty}^{\infty}dx\,\mathrm{Im}G^R_R(\xi_{\vec{q}},x)[n(x)-n(x+eV)]\times[f_1(x,\omega_{\vec{p}})+f_2(x,\omega_{\vec{p}})] \quad , \tag{2.17a}$$

$$f_1(x,\omega_{\vec{p}})\equiv[n(x+eV+\hbar\omega_{\vec{p}})+N(\hbar\omega_{\vec{p}})]g(x+eV+\hbar\omega_{\vec{p}}) \quad , \tag{2.17b}$$

$$f_2(x,\omega_{\vec{p}})\equiv[1-n(x+eV-\hbar\omega_{\vec{p}})+N(\hbar\omega_{\vec{p}})]g(x+eV-\hbar\omega_{\vec{p}}) \quad , \tag{2.17c}$$

$$g(u)\equiv[u\theta(u-\Delta)-u\theta(-u-\Delta)](u^2-\Delta^2)^{-1/2} \quad . \tag{2.17d}$$

In Eqs. (2.17), s denotes the spin of the tunneling carrier and Eq. (2.16) was constructed to give a phonon-assisted tunneling term directly compatible with the self-energy term. A better treatment of the momentum conservation rule has been given previously,[4] and is not thought to exert a major influence on our line shapes calculated for nearly dispersionless optical phonons.

In this subsection we are concerned about the effects of the superconducting metal electrode for a free-carrier model of the semiconductor. Thus, we introduce

$$\mathrm{Im}G^R_R(\xi_{\vec{q}},x)=-\pi\delta(\xi_{\vec{q}}-x) \quad , \tag{2.18}$$

which yields (performing the x integral prior to the $\xi_{\vec{q}}$ integral in analogy with Bennett *et al.*[4])

$$J_i(V,T)=\frac{4e\rho_{\parallel}}{h}\sum_{\vec{p},\vec{q}}|\Lambda^{(i)}(\vec{p})|^2\times\frac{\partial\xi_{\vec{q}}}{\partial q_\perp}[n(\xi_{\vec{q}})-n(\xi_{\vec{q}}+eV)]\times[f_1(\xi_{\vec{q}},\omega_{\vec{p}})+f_2(\xi_{\vec{q}},\omega_{\vec{p}})] \quad . \tag{2.19}$$

At $T=0$, after some manipulation, we obtain the simplified forms,

$$J_i(V,0)=\frac{2e\rho_{\parallel}}{\pi h}\textstyle\sum_{\vec{p}}|\Lambda^{(i)}(\vec{p})|^2\times[B_1(eV+\hbar\omega_{\vec{p}},-\zeta_R)+B_2(-eV+\hbar\omega_{\vec{p}},\zeta_R)+B_3(-eV+\hbar\omega_{\vec{p}},\zeta_R)] \quad , \tag{2.20a}$$

$$B_1(x,\zeta_R)\equiv\left[(\tfrac{1}{2}x+\zeta_R)(x^2-\Delta^2)^{1/2}+\tfrac{1}{2}\Delta^2\ln\left(\frac{-x+(x^2-\Delta^2)^{1/2}}{\Delta}\right)\right]\theta(-x-\Delta) \quad , \tag{2.20b}$$

$$B_2(x,\zeta_R) \equiv B_1(x,\zeta_R)\theta(x+\Delta+\zeta_R) \ , \tag{2.20c}$$

$$B_3(x,\zeta_R) \equiv [B_1(x,\zeta_R) - B_1(x+\zeta_R,0)] \times \theta(-x-\Delta-\zeta_R) \ . \tag{2.20d}$$

Consequently, if $\Lambda^{(i)}$ is independent of the bias voltage, then

$$G_i(V,0) \equiv \frac{dJ_i(V,0)}{d(eV)} = \frac{2e\rho_{\parallel}}{\pi h}\sum_{\vec{p}} |\Lambda^{(i)}(\vec{p})|^2 \times \{c_1(eV+\hbar\omega_{\vec{p}},\zeta_R)\theta(-eV-\hbar\omega_{\vec{p}}-\Delta) - c_1(eV-\hbar\omega_{\vec{p}},\zeta_R)[\theta(eV-\hbar\omega_{\vec{p}}-\Delta) \times \theta(-eV+\hbar\omega_{\vec{p}}+\Delta+\zeta_R)+\theta(eV-\hbar\omega_{\vec{p}}-\Delta-\zeta_R)] + c_1(eV-\hbar\omega_{\vec{p}}-\zeta_R,0)\theta(eV-\hbar\omega_{\vec{p}}-\Delta-\zeta_R)\} \ . \tag{2.21}$$

c_1 is given by Eq. (2.9b).

In the special case of dispersionless phonons, the phonon energies are given by

$$\hbar\omega_{\vec{p}} = \hbar\omega_0\Theta(p_c-p) \ , \tag{2.22a}$$

where p_c is the Debye-cutoff wave vector $p_c = (6\pi\rho)^{1/3}$. In this case, the remaining p integral in Eq. (2.21) is trivial as it gives only a normalizing constant.[5] Hence Eq. (2.21) yields an analytical expression for the tunnel conductance, the predictions of which are shown schematically in Fig. 4. The thresholds at $eV = \pm(\hbar\omega_0+\Delta)$ evidently arise from the θ functions in Eq. (2.21), which in turn reflect the dual requirements of energy conservation and the exclusion principle. The cusps shown in Fig. 4(b) do not result from Eq. (2.21), and are discussed in Sec. II C. The negative conductance for $eV > (\hbar\omega_0+\zeta_R+\Delta)$ is an interesting consequences of Eq. (2.21). It results because, at these large values of the bias, no additional tunneling channels open up with increasing bias since all of the electrons in the semiconductor already are emitting all possible phonons. Hence, since the barrier-penetration factor is constant in our model, for a normal metal the inelastic conductance vanishes for $eV > (\hbar\omega_0+\zeta_R+\Delta)$. However, for a superconducting metal, the superconducting-tunneling density of states constantly diminishes as the final state moves further from the Fermi energy. This diminution causes the negative values of G_i. In an actual junction, the bias dependence of the barrier-penetration factor causes a (usually much larger) increase in the conductance for $eV \geq \zeta_R$, which is expected to obscure the negative inelastic conductance.

Finally, if the effects of phonon dispersion are considered by using the model-phonon energies

$$\hbar\omega_{\vec{p}} = (\hbar\omega_0 - \alpha p^2)\Theta(p_c-p) \ , \tag{2.22b}$$

then the resulting evaluation of Eq. (2.21) must be performed numerically. The thresholds at $|eV| = (\hbar\omega_0+\Delta)$ broaden, and become highly asymmetric in the limit that electron and phonon damping is neglected. We illustrate these results in the section on numerical studies of the line shapes.

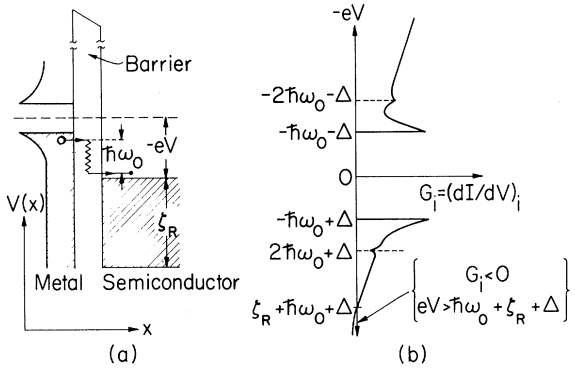

FIG. 4. (a) Schematic potential energy versus distance diagram for inelastic tunneling in a superconductor-semiconductor tunnel junction. Forward bias ($eV>0$) is defined when the metal is biased positively relative to the semiconductor. For dispersionless phonons of energy $\hbar\omega_0$, no inelestic current can flow until $|eV| \geq (\hbar\omega_0+\Delta)$ because of the combined effects of energy conservation and the exclusion principle. This is illustrated in the figure for $eV<0$, but also is true for $eV>0$ in which case the tunneling electrons at $eV=\hbar\omega_0+\Delta$ originate from the Fermi degeneracy in the semiconductor and terminate in the lowest empty quasiparticle state of the superconductor. The relevant initial state in the semiconductor lies at an excitation energy $\epsilon = -\hbar\omega_0$ when the bias is $eV=[(\hbar\omega_0+\Delta)+\hbar\omega_0]$. In this case, the phase-space restrictions in the semiconductor lead to an abnormally low initial density of tunneling states [see Figs. 3(b) and 3(c)]. Hence a cusplike minimum occurs in the tunnel conductance. A similar effect (with opposite sign) occurs at reverse bias $eV=-(2\hbar\omega_0+\Delta)$ due to the unusually large tunneling state density at $\epsilon=+\hbar\omega_0$. (b) The inelastic tunnel conductance associated with the junction illustrated in Fig. 4(a) if the barrier-penetration probability is independent of the bias voltage. The threshold effects at $|eV| = (\hbar\omega_0+\Delta)$ and the self-energy effects at $|eV| = (2\hbar\omega_0+\Delta)$ are shown. The effect of the superconductivity in the metal on the self-energy line shape is noted in the discussion of Fig. 3.

C. Combined Effects of Electrode Self-Energy Phenomena and Phonon-Assisted Tunneling

In the previous section, the evaluation of the inelastic current was performed for a general semiconductor electrode Green's functions until the introduction in Eq. (2.18) of the independent-electron spectral density. If, however, we invert the order of the $\xi_{\vec{q}}$ and x integrations, then by using the quasiparticle approximation, Eqs. (2.7), in Eqs. (2.17) we obtain

$$J_i(V,T)=\frac{2e\rho_{\parallel}}{\pi\hbar}\sum_{\vec{p}}|\Lambda^{(i)}(\vec{p})|^2 \times\int_{-\infty}^{\infty}dx\,[\xi(x)+\zeta_R]\Theta[\xi(x)+\zeta_R]Z(x) \times[n(x)-n(x+eV)][f_1(x,\omega_{\vec{p}})+f_2(x,\omega_{\vec{p}})]\,, \tag{2.23}$$

in which f_1 and f_2 are given by Eqs. (2.17b) and (2.17c). The important feature of Eq. (2.23) is its demonstration that the phase-space weighting factor, $\rho_{\parallel}[\xi(x)+\zeta_R]$, enters the inelastic current in a fashion analogous to its entrance in the elastic current Eq. (2.6). [The analogy would be exact if we were dealing with incoherent fluctuation-induced tunneling.[6] It is only approximate in Eq. (2.23) due to the approximate nature of (2.16).] The effect of quasiparticle dispersion on $\xi(x)$ is important only when $|x|\cong\hbar\omega_0$, for dispersionless phonons. Thus, as the relevant threshold effects in f_1 and f_2 occur when

$$|eV|\cong(\hbar\omega_0+\Delta+|x|)\,, \tag{2.24a}$$

we see that the combined self-energy inelastic threshold effects occur for

$$|eV|\cong 2\hbar\omega_0+\Delta\,, \tag{2.24b}$$

as sketched in Fig. 4(b).

It now is appropriate to recall that our primary interest lies in distinguishing between various mechanisms which can cause structure in the tunnel conductance near $|eV|\cong(\hbar\omega_0+\Delta)$. Consequently, we shall not consider further the combined influence of self-energy and inelastic tunneling effects resulting from the diagram in Fig. 1(b).

III. EVALUATION AND INTERPRETATION OF PREDICTED LINE SHAPES

In this section we present the results of numerical evaluations of the tunneling characteristic using simple models and parameters appropriate for the discription of metal contacts on boron-doped silicon.[6,7,14,18,19] We are interested primarily in two aspects of the model predictions: the nature of the changes in the line shapes when the metal electrode is driven from superconducting to normal by a magnetic field (at constant temperature), and the sensitivity of the predicted changes to the model parameters and approximations. The results of our investigations are presented by first demonstrating the qualitative distinction between the induced changes in the phonon-assisted tunneling line shapes and those in the line shapes associated with phonon-induced self-energy phenomena in the electrodes. We then discuss the dependence of the details of this distinction on the amount of dispersion of phonon spectrum and on the model used to describe the background one-electron tunneling. Finally, the temperature dependence in the line shapes is shown to provide further qualitative distinctions between the two mechanisms. We use deformation-potential models of the electron-phonon interactions, so that our numerical results are not representative of cases in which the electron-phonon vertex function has a strong dependence on momentum transfer.[4,6,7,9,15] Graphs of various line shapes are presented for $\Delta=1$ meV and $T=4.2\,^{\circ}$K. These parameters describe a typical metal electrode and a maximum feasible temperature at which to perform experiments illustrating the effects which we discuss. Therefore, our figures illustrate predictions for lower bounds on the type of phenomena one might expect to observe. The effects can become much larger at lower temperatures, i.e., as $\kappa T/\Delta\to 0$.

A comparison between the inelastic (phonon-assisted) tunneling line shapes and those associated with electrode self-energy effects is shown in Fig. 5. In calculating the curves shown in this figure, we use a model in which the one-electron barrier-penetration probability is taken to be a constant. Hence, the figure illustrates only many-body effects associated with electron-phonon coupling in an otherwise structureless barrier [Figs. 5(a) and 5(b)] and semiconductor electrode [Figs. 5(c) and 5(d)]. In the case of phonon-assisted tunneling, the major qualitative charges caused by the transition to a superconducting electrode are the sharpening of peaks in d^2I/dV^2, their shift (by an amount less than Δ) to higher values of the bias, and the sign reversal of the line shape for $|eV|\geq(\hbar\omega_0+\Delta)$. Qualitatively, identical line-shape changes occur for self-energy effects in the electrodes [Figs. 5(c) and 5(d)]. Quantitatively, two distinctions occur between the line shapes associated with the two effects. First, the shift of the line is considerably larger in the case of phonon-assisted (inelastic) tunneling. Second, the sign reversal at $|eV|>(\hbar\omega_0+\Delta)$ also is more pronounced for phonon-assisted tunneling.

In order to assess the significance of these distinctions for the analysis of experimental data, we must study their dependence on the model used in the calculation. The most important modification of the simple phonon-assisted-tunneling calculation, whose consequences are shown in Fig. 5(a), is the incorporation of the influence of phonon dispersion. In Fig. 5(b), we show the predictions of a model calculation in which these dispersion effects have been incorporated in such a fashion as to place an upper bound on them. The phonon spectrum given by Eq. (2.22b) was used in the evaluation of the $\vec{p}$ integral

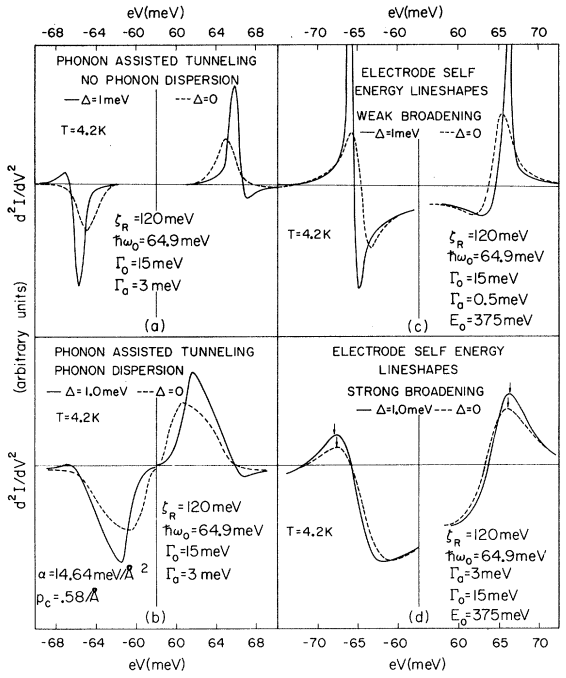

FIG. 5. (a) Phonon-assisted d^2I/dV^2 line shapes resulting from Eqs. (2.23) and (2.22a) (no phonon dispersion) in the vicinity of $\pm\hbar\omega_0$ ($\hbar\omega_0 = 64.9$ meV, the optical-phonon energy in silicon). The line shapes are characteristic of the inelastic tunneling thresholds treated in Sec. II B. The self-energy effects on these line shapes only appear when $|eV| \cong 2\hbar\omega_0$, as discussed in Sec. II C. (b) Phonon-assisted d^2I/dV^2 with optical-phonon dispersion included according to Eq. (2.22b). $|\Lambda^{(i)}(\vec{p})|^2$ in Eq. (2.23) was taken to be a constant in the numerical calculations. Phonon dispersion has a triple effect upon Fig. 5(a): The line shapes are broadened; they are made asymmetric, and the difference between the normal and superconducting line shapes is greatly reduced. (c) d^2I/dV^2 resulting from self-energy effects calculated according to Eqs. (2.10a) and (2.10b) (full propagator) with $\Gamma_a = 0.5$ meV. The electronic self-energy is given by Eqs. (A2.2)–(A2.6) of Davis and Duke.[7] (d) Self-energy-effect d^2I/dV^2 line shapes calculated with the full propagator, as in Fig. 5 (c), with the distinction that $\Gamma_a = 3$ meV here. Increasing Γ_a broadens the line shapes and diminishes the differences between the normal and and superconducting curves. Arrows in the figures indicate the highest points in the corresponding curves and serve to mark the superconducting shift. The light-hole effective mass in the silicon electrode is taken[20] to be $m_R = 0.16m$. The free-electron model is used to describe the normal-metal electrode.

in Eq. (2.21). The value of α is chosen to give approximately a 5-meV dispersion in the LO phonon spectrum from Γ to $p_c \equiv 0.58$ Å^{-1}. Thus, $\hbar\omega(p_c) = 60$ meV, $\alpha = 14.64$ meV/Å^2, and we take $\Lambda^{(i)}(\vec{p})$ to equal a constant, i.e.,

$$\sum_{\vec{p}} |\Lambda^{(i)}(\vec{p})|^2 \to [|\Lambda^{(i)}|^2/(2\pi^2)] \int_0^{p_c} p^2\, dp \,. \quad (3.1)$$

The consequences of this model are shown in Fig. 5(b). The peak in the d^2I/dV^2 curve is shifted to lower energies. The sign reversal in the line shape at $|eV| > (\hbar\omega_0 + \Delta)$ when the metal electrode becomes superconducting is reduced substantially, as is the narrowing of the main peaks. Our model is expected to overestimate the influence of dispersion on the line shape because $|\Lambda(\vec{p})|$ probably is much smaller for large values of $\vec{p}$ than near $\vec{p} = 0$. Hence, since both the sharpening of the line shape and its sign reversal at $|eV| > (\hbar\omega_0 + \Delta)$ are still prominant features in Fig. 5(b), we conclude that these features of the line shape are characteristic of optical-phonon-assisted tunneling in metal-silicon contacts.

Turning to the case of self-energy induced resonance structure at $|eV| \cong \hbar\omega_0$, we see from Figs. 5(c) and 5(d) that, at forward bias ($eV > 0$), the qualitative features of the line shapes for either the normal or superconducting metal contact do not differ substantially from those predicted by the phonon-assisted-tunneling mechanism. The analytical origin of this result resides in the sharp increase at the phonon-emission threshold of the imaginary part of the electronic self-energy of a carrier in the semiconductor electrode. As demonstrated by Duke,[17] this increase creates a corresponding increase in the conductance at $|eV| \cong \hbar\omega_0$ in addition to the cusplike behavior associated with the quasiparticle approximation as shown, e.g., in Fig. 3. However, the size of this increase in the conductance is small unless $eV = \hbar\omega_0 \cong \zeta_R$. This situation occurs at forward bias in metal contacts on a variety of degenerate semiconductors. Consequently, at forward values of the bias in these units, the self-energy line shape exhibits a threshold behavior which resembles a phonon-assisted-tunneling line shape but which is not antisymmetric about zero bias. One of the reasons for our interest in studies of the change in the line shape when the metal electrode is a superconductor is the potential utilization of this change to remove within the framework of the transfer-Hamiltonian model such ambiguities in the identification of observed line shapes with microscopic mechanisms.

Two phenomena influence substantially the nature of the increase at $\epsilon \cong \hbar\omega_0$ in $\mathrm{Im}\Sigma(\epsilon)$ for the carrier in the semiconductor: optical-phonon dispersion and electron damping due to other scattering mechanisms. After some numerical studies of both phenomena, Davis and Duke[7] concluded that as the extent of the phonon dispersion $\Delta\omega = [\omega(p_c) - \omega(0)]$ and the magnitude of the energy width Γ_α due to acoustical-phonon scattering satisfied Γ_α and $\Delta(\hbar\omega) \ll \hbar\omega_0$, a simple phenomenological de-

scription could be used to describe the consequences of the finite width of the increase in $\mathrm{Im}\Sigma$ ($|\epsilon| \gtrsim \hbar\omega_0$). In order to reduce computing time, we have followed their prescription and set

$$\ln[\zeta_R^{1/2} - \epsilon_\pm^{1/2}] \to \tfrac{1}{2}\ln[(\zeta_R^{1/2} - \epsilon_\pm^{1/2})^2 + \Gamma_a^2/4\zeta_R] \ , \quad (3.2a)$$

$$\pi\Theta(\pm\epsilon - \hbar\omega_0) \to \tfrac{1}{2}\pi + \tan^{-1}[(\pm\epsilon - \hbar\omega_0)/\Gamma\alpha] \ , \quad (3.2b)$$

in the expressions for the electronic self-energy given by Eqs. (A2.4) in Ref. 7. Using this prescription, we obtain the results shown in Fig. 5(c) for weak damping plus dispersion, i.e., $\Gamma_a = 0.5$ meV, and Fig. 5(c) for strong damping plus dispersion, i.e., $\Gamma_a = 3$ meV. As we might have anticipated, the narrowing and shift of the resonant line shape can be reduced substantially by increasing Γ_a. However, the important feature of Fig. 5 is its illustration that the sign reversal at $|eV| > (\hbar\omega_0 + \Delta)$ of the line shape is a characteristic feature of phonon-assisted tunneling, whereas for the electrode-self-energy effect it is small at best, and can be eliminated almost completely by increasing Γ_a.

A final variable on which the resonant line shapes depend is the shape of the independent-electron background conductance. In the case of phonon-assisted tunneling, the magnitude of any asymmetry about zero bias in the threshold conductance is proportional to the asymmetry in the magnitude of the one-electron current at $eV = \pm\hbar\omega_0$ (see e.g., Bennett, Duke, and Silverstein[4]). Numerically, these asymmetries have been found to be small in the cases for which they have been calculated.[4] However, the influence of the background conductance on the self-energy-induced resonant line shapes often is not small for parameters characterizing metal-semiconductor tunnel junctions.[7,17] To illustrate this influence, it is convenient and informative first to demonstrate the effect of the quasiparticle approximation on the line shape and subsequently to investigate the quasiparticle line shapes predicted by different models of the one-electron barrier-penetration probability. The transition from the complete propagator to the quasiparticle approximation (QPA) within the constant-barrier model is illustrated in Figs. 6(a) and 6(b). Note in particular how the extra increase in the conductance at $|eV| \cong \hbar\omega_0$ associated with an increase in $\mathrm{Im}\Sigma(\epsilon) \cong \hbar\omega_0$ smooths out the minima in d^2I/dV^2 for $|eV| \lesssim \hbar\omega_0$. The absence of these minima is a prominent feature of the experimental data[18] for metal contacts on Si:B. This absence requires the abandonment of the QPA in the data analysis for these systems.[7] However, the change in the line shape between normal and superconducting contacts is relatively insensitive to the use of the QPA. In this application, the only systematic

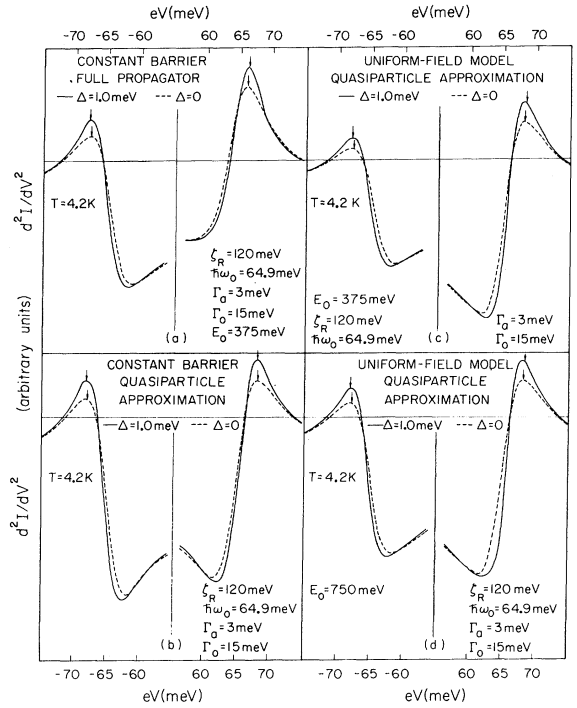

FIG. 6. (a) Self-energy-effect d^2I/dV^2 line shapes as shown in Fig. 5 (d) but on a larger scale. Including the full $\mathrm{Im}\,\Sigma(x)$ in the calculations reduces the dip in forward bias compared to the quasiparticle approximation and introduces a crossover between the normal and superconducting line shapes at $|eV| \cong +70$ meV. In all panels of this figure, the electronic self-energy was evaluated using Eqs. (A2.2)–(A2.6) given by Davis and Duke.[7] (b) d^2I/dV^2 calculated from Eq. (2.8a) (the quasiparticle approximation) with $D_0(E_\parallel) = D_0$ (constant-barrier model). Forward- and reverse-bias line shapes are approximately the same size; the dip at $|eV| < \hbar\omega_0$ observed in reverse bias is lower than that in forward bias. (c) d^2I/dV^2 calculated according to Eq. (2.8a) with $D_0(E_\parallel) = D_0\exp(-E_\parallel/E_0)$ (the uniform-field model), $E_0 = 375$ meV. (d) d^2I/dV^2 calculated in the uniform-field model and quasiparticle approximation with $E_0 = 750$ meV. Increasing E_0 enhances the scale of the reverse bias structure relative to that of the structure at forward bias. Arrows indicate positions of peaks of corresponding curves. The light-hole mass in the silicon electrode is taken[20] to be $m_R = -0.16m$. The free-electron model was used to describe the normal-metal electrode.

flaw of the QPA seems to be its underestimation of the sign reversal for $|eV| > (\hbar\omega_0 + \Delta)$: an effect which is small for the self-energy line shapes anyway.

Using the QPA, the influence of the shape of the one-electron barrier-penetration probability on the self-energy line shapes is illustrated in panels Figs 6(b)–6(d). The uniform-field model[6]

$$D(E_\parallel) = D_0 e^{-E_\parallel/E_0} \quad (3.3)$$

is used in the construction of panels Figs. 6(c) and 6(d). The major effect of varying E_0 (recall that $E_0 \to \infty$ gives the constant-barrier model) is the decrease in the magnitude of the reverse bias resonance with decreasing E_0. The change in the line shapes for normal as opposed to superconducting metal electrodes is quite insensitive to the model used for $D(E_{\parallel})$. It is noteworthy that, although the *positions* of the maxima in d^2I/dV^2 depend on the approximations used in the analysis [contrast Fig. 6(a) with Fig. 6(b)], the normal-superconducting *shift* of the position of these maxima is both small and insensitive to the model approximations.

The temperature dependence of the resonant line shapes as well as their bias dependence serves to distinguish between boson-assisted tunneling and self-energy effects. The inelastic d^2I/dV^2 line shapes calculated from Eqs. (2.23) and (2.22a) (no dispersion) are dominated at $|eV| \cong \hbar\omega_0$ by the dual requirements of energy conservation and the exclusion principle as discussed in Sec. II B. The effect on the inelastic tunneling line shapes of increasing T is only the broadening of the line shapes. For normal metal electrodes, the maxima and minima in forward and reverse bias, respectively, do not change their voltage positions. The maxima and minima of the corresponding superconducting-electrode curves vary in eV only as $\Delta(T)$. This is demonstrated in Fig. 7(a), where the line shapes are calculated in reverse bias and $\Delta(T)$ is assumed to vary as the BCS gap parameter [$\Delta(0) = 1.34$ meV, appropriate for Pb, and $T_c = 8.85$ °K]. We define

$$V_{\mathrm{INS}} \equiv V_{\mathrm{PSI}} - V_{\mathrm{PNI}} , \tag{3.4a}$$

$$P_{\mathrm{INS}} \equiv |P_{\mathrm{SI}} - P_{\mathrm{NI}}| . \tag{3.4b}$$

V_{PSI} (V_{PNI}) is the reverse bias position of the inelastic superconducting (normal) d^2I/dV^2 minimum, and $P_{\mathrm{SI}}(P_{\mathrm{NI}})$ is the magnitude of the corresponding minimum. ΔV_{INS} follows the temperature dependence of the BCS gap parameter. The ΔP_{INS} curve illustrates the broadening of the line shapes as well as the decrease in the magnitude of the superconductor's line shape with respect to the normal line shape as $\Delta(T) \to 0$, i.e., $(T \to T_c)$. Error bars in ΔV_{INS} result from the finite voltage increments (0.1 meV) used in the numerical computation.

The normal-electrode self-energy line shape exhibits a markedly different temperature dependence from the corresponding boson-assisted line shape. As T increases so that $\kappa T > \Gamma_a$, the normal resonant peaks shift in voltage as well as broaden. The analytic origin of this temperature behavior is easily seen when we examine the line shape in the quasiparticle approximation. From Eqs. (2.8a) –(2.8d) we get using the constant-barrier model and $\Delta = 0$:

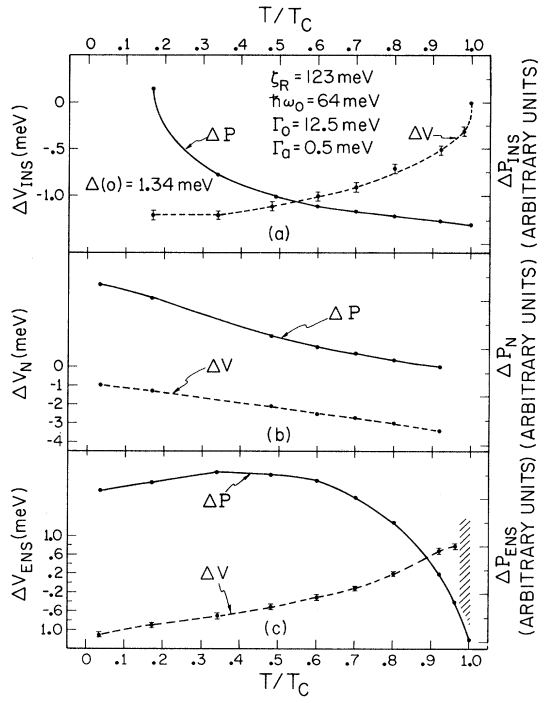

FIG. 7. (a) Reverse bias inelastic normal-superconducting voltage shift (ΔV_{INS}) and peak difference (ΔP_{INS}) computed numerically from Eqs. (2.23) and (2.22a) (no dispersion) as functions of temperature. $\Delta V_{\mathrm{INS}} \equiv V_{\mathrm{PSI}} - V_{\mathrm{PNI}}$; $\Delta P_{\mathrm{INS}} \equiv |P_{\mathrm{SI}} - P_{\mathrm{NI}}|$ [see the discussion following Eqs. (3.4) for definitions]. The gap parameter $\Delta(T)$ has the BCS temperature dependence[21] with $\Delta(0) = 1.34$ meV (appropriate for Pb), $T_c = 8.85$ °K. (b) Reverse bias self-energy normal-electrode line-shape width (ΔV_N) and peak-to-valley height (ΔP_N) computed numerically from Eqs. (2.11a)–(2.11c) (full propagator and constant barrier) as functions of temperature $\Delta V_N \equiv V_{\mathrm{PN}} - V_{\mathrm{VN}}$; $\Delta P_{\mathrm{N}} \equiv |P_{\mathrm{PN}} - P_{\mathrm{VN}}|$ [see discussion following Eqs. (3.7) for definitions]. $\Delta(T)$ is the BCS gap parameter[21] with $\Delta(0) = 1.34$ meV and $T_c = 8.85$ °K. The parameter used are the same as those in Fig. 7(a). (c) Reverse bias self-energy normal superconducting voltage shift (ΔV_{ENS}) and peak difference (ΔP_{ENS}) computed numerically from Eqs. (2.11a)–(2.11c) (full propagator and constant barrier) as functions of temperature. $\Delta V_{\mathrm{ENS}} \equiv V_{\mathrm{PS}} - V_{\mathrm{PN}}$; $\Delta P_{\mathrm{ENS}} \equiv |P_{\mathrm{PS}} - P_{\mathrm{PN}}|$ [see discussion following Eqs. (3.8) for definitions]. $\Delta(T)$ is the BCS gap parameter[21] with $\Delta(0) = 1.34$ meV. $T_c = 8.85$ °K. The parameters used are the same as those in Fig. 7(a). The cross-hatching indicates the region where the superconducting peak splits. The negative voltage shift for $T \leq T_c$ results from the normal line shape's temperature behavior, as discussed in Sec. III. Error bars indicate uncertainty in the voltage produced by the finite bias increments (0.1 meV) used in the numerical computations.

$$G_e(V,T) = -(2e\rho_{\parallel}D_0/h)\int_0^{\infty} dy\, n'(y)[\xi(y-eV)+\zeta_R] \times \theta[\zeta_R+\xi(y-eV)] \tag{3.5a}$$

and

$$\frac{dG_e}{d(eV)}(V,T) = I_1 + I_2 \ , \tag{3.5b}$$

$$I_1 \equiv -(2e\rho_{\parallel}D_0/h)n[x(-\zeta_R)+eV] \ , \tag{3.5c}$$

$$I_2 \equiv -(2e\rho_{\parallel}D_0/h)\int_{x(\zeta_R)+eV}^{\infty} dy\, n'(y)\frac{d}{dy}\,\mathrm{Re}\Sigma(y-eV) \ . \tag{3.5d}$$

I_1 represents only the constant background; the resonant structure results from I_2. If $z \equiv y/\kappa T$,

$$I_2 \cong \frac{2e\rho_{\parallel}D_0}{h\kappa T}\int_{-\infty}^{\infty} dz\,\frac{e^z}{(1+e^z)^2}\frac{d}{dz}\,\mathrm{Re}\Sigma(z\kappa T - eV) \ . \tag{3.6}$$

As T increases, the absolute magnitude of I_2 decreases and the scale of the structure in $(d/dz)\,\mathrm{Re}\Sigma$ (for $|z\kappa T - eV| \cong \hbar\omega_0$) decreases along the z axis. This means that the negative portion of $(d/dz)\,\mathrm{Re}\Sigma$ contributes to the integral at high $T[\kappa T > \Gamma_a$, since $\Gamma_a \sim$width of structure in $(d/dy)\,\mathrm{Re}\Sigma]$, so that the maximum value of I_2 occurs at larger $|eV|$. The net result is a shift of the peak in d^2I/dV^2 to higher $|eV|$. For larger Γ_a, the temperature behavior of the shift will be smaller.

The net result is illustrated in Fig. 7(b). The values of d^2I/dV^2 described by the figure are calculated from Eqs. (2.11a)–(2.11c) (full propagator and constant barrier) in reverse bias for normal metal electrodes ($\Delta = 0$). The quantities plotted in the figure are defined by

$$\Delta V_N \equiv V_{PN} - V_{VN} \ , \tag{3.7a}$$

$$\Delta P_N \equiv |P_{\mathrm{PN}} - P_{\mathrm{VN}}| \ , \tag{3.7b}$$

with $V_{\mathrm{PN}}(V_{\mathrm{VN}})$ denoting the reverse bias portion of the normal self-energy d^2I/dV^2 peak (valley) and P_{PN} (P_{VN}) the magnitude of the peak (valley). As T increases ΔV_N increases and ΔP_N decreases, as explained in the discussion of Eq. (3.6). The parameters used to calculate Fig. 7(b) are the same as those used in Fig. 7(a).

The temperature dependence of the normal self-energy line shape exerts the dominant influence on the normal-superconducting voltage shift. Let us define

$$\Delta V_{\mathrm{ENS}} \equiv V_{\mathrm{PS}} - V_{\mathrm{PN}} \ , \tag{3.8a}$$

$$\Delta P_{\mathrm{ENS}} \equiv |P_{\mathrm{PS}} - P_{\mathrm{PN}}| \ , \tag{3.8b}$$

in which V_{PS} is the reverse bias position of the self-energy d^2I/dV^2 peak for a superconducting metal electrode and P_{PS} is the magnitude of this peak. V_{PN} and P_{PN} are defined as they are in Eqs. (3.7a) and (3.7b).

Since the superconducting density of states diverges at $x = \Delta(T)$, V_{PS} varies in temperature ($T < T_c$) only as $\Delta(T)$ (which we have taken to be the BCS gap parameter). Thus, as T increases [$\Delta(T)$ decreases] the peak of the superconducting line shape moves towards the center of the reverse bias structure. The normal peak, however, moves away from the center as T increases. Thus, ΔV_{ENS} may change sign for sufficiently large values of T. In addition, when $T \sim T_c$ the superconducting line shape exhibits two peaks, one resulting from the superconducting density of states and the other from the normal component. In this region, it is impossible to define ΔV_{ENS}.

This behavior is illustrated in Fig. 7(c). The values of d^2I/dV^2 used to obtain the figure are calculated from Eqs. (2.11a)–(2.11c) (full propagator and constant barrier) in reverse bias. The cross-hatching indicates the region where the superconducting peak splits. The peak in ΔP_{ENS} results from the BCS gap's slow variation, so that the superconducting peak changes little, while the normal line shape varies in temperature according to Eq. (3.6a). For large values of Γ_a, the normal line shape changes more slowly, so that all these effects are reduced.

No attempt was made to fit experimental values of the temperature dependence because they were available only for one sample. Data taken on this sample[22] are consistent with the model predictions described above.

Summarizing, we conclude from Figs. 5 and 6 that at a given temperature inelastic tunneling and self-energy effects are distinguishable for a variety of models on the basis of two features of the predicted line shapes. First, the shift in the position of the maximum in d^2I/dV^2 is consistently larger for inelastic tunneling than for self-energy effects. Second, a substantial sign reversal of the resonant line shape occurs when $|eV| > (\hbar\omega_0 + \Delta)$ in the case of inelastic tunneling, whereas this reversal is either small or absent in the case of self-energy effects. Other features of the d^2I/dV^2 line shapes, e.g., the dip in the self-energy resonance at $|eV| < \hbar\omega_0$, appear to be sufficiently model dependent that their utilization as a test for the self-energy mechanism should be approached with caution. However, the temperature dependence of the d^2I/dV^2 line shapes, illustrated in Fig. 7, also provides a qualitative distinction between the self-energy and inelastic-tunneling mechanisms.

IV. SYNOPSIS AND DISCUSSION

In Sec. II, we derived expressions for the current in a superconductor-semiconductor tunnel junction due to boson-assisted tunneling as well as for the usual elastic current in the presence of

electron-boson interactions in the semiconductor electrode. Explicit expressions for the tunnel conductance were quoted in the limits that (a) the boson excitation spectrum is dispersionless, (b) the electron-boson interaction is independent of momentum transfer, and (c) the independent-electron barrier-penetration probability is a constant. Electron-hole symmetry in the semiconductor is not used in these derivations or in our numerical analyses. In Sec. III, we extended the analysis to include the effects of boson dispersion and energy-dependent barrier-penetration probabilities. The numerical examples presented in Sec. III were designed to interpret data[18,22] taken for In and Pb contacts on Si:B. They revealed that (i) the shift to higher bias of the resonant maxima in d^2I/dV^2 at $|eV| = \hbar\omega_0$, and (ii) the sign reversal of the resonant line shapes at $|eV| \gtrsim (\hbar\omega_0 + \Delta)$ when the metal electrode becomes superconducting (i.e., a quenching magnetic field is removed at a constant temperature) are much larger for inelastic tunneling than for the resonant self-energy effect.

A comparison of the model predictions with some data[22] for Pb contacts on oxide-coated Si:B is shown in Fig. 8. The description of this experimental data is reasonably good. However, no attempt was made to fit the forward bias line shapes, because there is evidence to suspect that some phonon-assisted tunneling is occurring in parallel with the elastic channel at forward bias.[18] In addition, the reverse bias resonant line shape depends explicitly on the doping level of the semiconductor[18] for $N_a < 10^{20}$ cm^{-3}. These results suggest that the mechanism (s) causing the resonant line shapes may be more complicated than a simple electrode self-energy effect when the doping is sufficiently small that a significant space-charge region exists inside the semiconductor electrode. Consequently, we are attempting to generalize our analysis of these junctions to describe the case in which both the inelastic tunneling and self-energy effects are caused by impurities localized near the surface of semiconductor electrode. Such a hypotheseis seems capable of describing both of the mysteries in the existing data; i.e., a substantial doping dependence of the reverse bias line shape and the preferential occurrence of inelastic tunneling at forward bias.

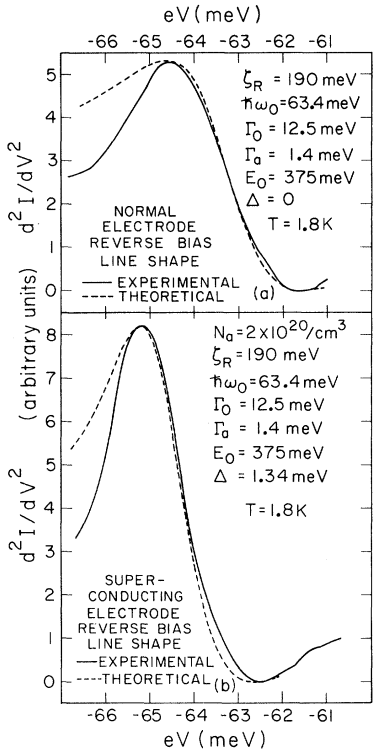

FIG. 8. (a) Theoretical and experimental resonant reverse bias line shapes for normal Pb contacts on oxide-coated boron-doped Si.[22] The normal-metal peak occurs at 64.6 ± 0.2 meV in reverse bias. $N_a = 2 \times 10^{20}$ cm^{-3} is the impurity concentration and ζ_R is calculated in the three-band model.[18] The theoretical line shape was calculated with the full propagator in the constant-barrier model [Eqs. (2.10a) and (2.10b) with parameters appropriate to the experiment]. $\hbar\omega_0 = 63.4$ meV was chosen to account for the effects of phonon-dispersion on $\Sigma(\epsilon)$.[7] (b) Theoretical and experimental resonant reverse bias d^2I/dV^2 line shapes for superconducting Pb contacts on boron-doped silicon.[22] The lead electrode becomes superconducting when the quenching field ($H = 4$ kG) is removed. The superconducting peak occurs at -65.2 ± 0.2 meV in reverse bias. N_a is the impurity concentration and ζ_R is calculated in the three-band model.[18] $\Delta = 1.34$ meV is the $T = 0$ superconducting energy gap for Pb. The theoretical line shape was calculated with the full propagator in the constant-barrier model [Eqs. (2.10a) and (2.10b)].

ACKNOWLEDGMENTS

The authors are indebted to Dr. L. C. Davis for the use of his computer programs for the electronic self-energy and to Dr. D. Cullen and L. Schein for the use of their data prior to publication.

*Work supported in part by the Advanced Research Projects Agency under Contract No. SD-131.

[1]J. Bardeen, Phys. Rev. Letters 6, 57 (1961).

[2]M. H. Cohen, L. M. Falicov, and J. C. Phillips, Phys. Rev. Letters 8, 316 (1962).

[3]C. B. Duke, S. D. Silverstein, and A. J. Bennett, Phys. Rev. Letters 19, 312 (1967).

[4]A. J. Bennett, C. B. Duke, and S. D. Silverstein, Phys. Rev. 176, 969 (1968).

[5]C. B. Duke, in *Proceedings of the International Sum-*

mer School on Electron Tunneling Phenomena in Solids, Risö, 1966 (Plenum, New York, 1969), pp. 405–426.
[6]C. B. Duke, *Tunneling in Solids* (Academic, New York, 1969), Chaps. 6 and 7.
[7]L. C. Davis and C. B. Duke, Phys. Rev. 184, 764 (1969).
[8]L. C. Davis, Phys. Rev. 187, 1177 (1969).
[9]C. B. Duke, Phys. Rev. 186, 588 (1969).
[10]I. Giaever and H. R. Zeller, Phys. Rev. Letters 20, 1504 (1968).
[11]H. R. Zeller and I. Giaever, Phys. Rev. 181, 789 (1969).
[12]A. A. Abrikosov, L. P. Gor'kov, and I. E. Dzyaloshinskii, *Methods of Quantum Field Theory in Statistical Physical* (Prentice-Hall, Englewood Cliffs, N. J., 1963), pp. 308, 315–317, 327–334.
[13]C. B. Duke, Phys. Rev. 168, 816 (1968).
[14]L. C. Davis and C. B. Duke, Solid State Commun. 6, 193 (1968).
[15]C. B. Duke, M. J. Rice, and F. Steinrisser, Phys. Rev. 181, 733 (1969).
[16]K. L. Ngai, E. N. Economou, and M. H. Cohen, Phys. Rev. Letters 22, 1375 (1969).
[17]C. B. Duke, Ref. 6, Sec. 20b. See, especially, Eq. (20.18). Unfortunately, in Eq. (20.4) of this reference, one should replace D_0 by $2D_0$. This fact leads to an error by a factor of 2 in Eq. (20.18). This error is corrected in the equations given in the present paper.
[18]D. Cullen, Ph. D. thesis, University of Illinois, 1969 (unpublished).
[19]E. L. Wolf, Phys. Rev. Letters 20, 204 (1968).
[20]R. A. Smith, *Semiconductors* (Cambridge U. P., London, 1961), p. 350.
[21]J. M. Blatt, *Theory of Superconductivity* (Academic, New York, 1964), p. 244.
[22]L. Schein (private communication).

PHYSICAL REVIEW B VOLUME 2, NUMBER 5 1 SEPTEMBER 1970

Transition Temperature of Superconducting Indium, Thallium, and Lead Grains

J. H. P. Watson
Research and Development Laboratories, Corning Glass Works, Corning, New York 14830
(Received 21 November 1969)

Experimental results on the transition temperature of indium, thallium, and lead grains of various sizes, together with preliminary measurements on other metals, can be interpreted in terms of changes in the phonon spectrum which alter the electron-phonon coupling constant, although some anomalies exist.

In this paper, measurements of the superconducting transition temperature of indium and thallium in porous glass are presented. The samples are produced by forcing molten metal into the porous structure, as described in the literature.[1,2] The pore diameter d was determined by mercury porosimetry,[2,3] and the values obtained were in agreement with those obtained from electron microscope pictures of the structure. The metal in the porous glass has been described as being in the form of spherical grains of closely equal size.[4]

The critical fields of metals in porous glass behave like granular superconductors.[2,5,6] In such a system the electron mean free path l is of the form $l = d\tau$, where d is the grain diameter and τ is the transmission probability of the electron between grains. For indium in normally prepared porous glass, $\tau \sim 0.03$.[2] The metal grains produced in this way are highly crystalline, as shown by the sharpness of the x-ray diffraction lines. This indicates that in these samples surface or size effects dominate, as distinct from the films evaporated at low temperature, where amorphousness of the metal lattice is an extra complication.

The transition temperature T_c was located by a mutual inductance technique as the temperature at which the imaginary part χ'' of the complex susceptibility $\chi(=\chi' + i\chi'')$ begins to change.[1] Measured in this way, T_c is independent of the amplitude of the ac field up to 20 Oe. The value used here was 1 Oe. The transition width ΔT_c was about 0.05 °K wide. Hake[7] has recently shown that fluctuation effects in samples with small values of $\xi_0 l$ can produce changes in resistivity above T_c. In view of this, the values of T_c obtained here could be lower by an amount of order ΔT_c.

Recently, McMillan[8] showed that the transition temperature of simple metals could be increased by a reduction of Θ_D, the Debye temperature. It has been suggested[9–11] and confirmed experimentally[12] that in small crystallites the phonon spectrum is appreciably altered by a greater proportion of low-frequency surface phonons, and it has been suggested that this is the cause of the shifts in T_c in granular or disordered materials.

Garland *et al.*[9] have derived the following equation for T_c:

$$\ln \frac{\langle\omega^2\rangle^{1/2}\omega_{0b}}{1.26 T_c \langle\omega_b^2\rangle^{1/2}} = \frac{1+\lambda}{A(1-0.5\mu^*)\lambda - \mu^*} , \qquad (1)$$